Quantitative flow analysis of swimming dynamics with coherent Lagrangian vortices

F. Huhn, W. M. van Rees, M. Gazzola, D. Rossinelli, G. Haller, and P. Koumoutsakos

Quantitative flow analysis of swimming dynamics with coherent Lagrangian vortices

F. Huhn,[1,a)] W. M. van Rees,[2] M. Gazzola,[3] D. Rossinelli,[2] G. Haller,[1] and P. Koumoutsakos[2]

[1]*Department of Mechanical and Process Engineering, Institute of Mechanical Systems, ETH Zürich, Leonhardtstrasse 21, CH-8092 Zurich, Switzerland*
[2]*Chair of Computational Science, ETH Zürich, Clausiusstrasse 33, CH-8092 Zürich, Switzerland*
[3]*School of Engineering and Applied Sciences, Harvard University, Cambridge, Massachusetts 02138, USA*

Undulatory swimmers flex their bodies to displace water, and in turn, the flow feeds back into the dynamics of the swimmer. At moderate Reynolds number, the resulting flow structures are characterized by unsteady separation and alternating vortices in the wake. We use the flow field from simulations of a two-dimensional, incompressible viscous flow of an undulatory, self-propelled swimmer and detect the coherent Lagrangian vortices in the wake to dissect the driving momentum transfer mechanisms. The detected material vortex boundary encloses a Lagrangian control volume that serves to track back the vortex fluid and record its circulation and momentum history. We consider two swimming modes: the C-start escape and steady anguilliform swimming. The backward advection of the coherent Lagrangian vortices elucidates the geometry of the vorticity field and allows for monitoring the gain and decay of circulation and momentum transfer in the flow field. For steady swimming, momentum oscillations of the fish can largely be attributed to the momentum exchange with the vortex fluid. For the C-start, an additionally defined jet fluid region turns out to balance the high momentum change of the fish during the rapid start. © 2015 AIP Publishing LLC. [http://dx.doi.org/10.1063/1.4919784]

Lagrangian coherent structures (LCSs) characterize fluid transported coherently inside a vortex and can help elucidate the governing mechanisms of momentum transfer in a flow field. We use the dynamics of the LCS to characterize the flow field and propulsion mechanism of an anguilliform swimmer employing different swimming modes.

I. INTRODUCTION

The way swimmers take advantage of the surrounding liquid environment is subtle and its governing mechanisms remain elusive to a large extent. Fishes propel themselves by deforming their bodies to transfer momentum to the surrounding fluid. Both for fast starts and steady-state swimming, their body strokes correspond to sequences of acceleration and deceleration. The continuously alternating rates of momentum transfer, both globally in the entire flow field and locally along the body surface, make it difficult to separate thrust and drag forces.[1,20] This complicates our understanding of the hydrodynamic mechanisms underlying self-propulsion in swimming.

Understanding the momentum transfer between the swimmer and the flow structures in its wake holds the promise of elucidating the fundamental physical mechanisms governing fish swimming.[2,3] In order to extract the information as to when and where the swimmer accelerates its

surrounding fluid, we rely on the detection and tracking of LCSs. LCSs are persistent material objects in the flow that characterize the fluid deformation over a certain period of time.[9,10] LCSs are composed of finite-time Lagrangian trajectories of fluid particles, obtained from the application of concepts of dynamical systems theory to Lagrangian fluid motion. Haller[9] reviews various types of LCS and shows a number of applications to geophysical flows.

In the context of fish propulsion, LCSs have been used to reveal the flow topology of several flapping propulsion devices using experimental and numerical data. Peng et al.[16] construct a boundary of an isolated vortex pair by combining attracting and repelling hyperbolic LCSs, based on finite-time Lyapunov exponents (FTLE), in order to estimate propulsive forces. In a follow-up article, Peng and Dabiri[17] study a numerical simulation of a self-propelled flexible plate and compute hyperbolic FTLE-based LCSs. They define an upstream wake and use the area enclosed by the LCSs to determine an unsteady mass flow rate past the swimmer. Green et al.[7] use experimental flow data of a pitching panel, mimicking a caudal fish fin. The transition of the wake topology for increasing Strouhal number is shown by means of FTLE-based hyperbolic LCS. All three studies detect LCSs as FTLE ridges, while by now, a precise definition of a hyperbolic LCS is available that returns a coherent material line.[8]

In the first two studies, the authors attempt to track fluid enclosed by FTLE ridges. For the tracking of a coherent fluid region, this approach seems problematic, since hyperbolic structures stretch exponentially under the flow and are therefore unable to define a closed vortex boundary that evolves coherently under the flow. Moreover, FTLE ridges do not

a)Now at Department of Experimental Methods, German Aerospace Center (DLR), Institute of Aerodynamics and Flow Technology, Göttingen, Germany. Electronic mail: florian.huhn@imes.mavt.ethz.ch.

form closed loops, and rather spiral into coherent vortices, incorrectly suggesting the lack of a coherent core in these cases. Even if closed curves are constructed from FTLE ridges computed in forward and backward time direction, the ridge curves neither close up, and the curves have to be closed manually.[16] As an additional drawback, the material flux across an FTLE ridges is generally non-zero.[8,9] If consecutive snapshots of FTLE ridges are used to define an evolving boundary, fluid is flowing into and out of the tracked fluid region, so that the Lagrangian property is lost.

In contrast to FTLE ridges that only roughly identify *hyperbolic* structures in the flow, our novel method[11] detects *elliptic* LCS, denoted by *coherent Lagrangian vortices*. The resulting closed material line has a zero material flux across it by construction. This is a key property for the quantification of momentum exchange between the engulfed fluid and the swimming body. The obtained material vortex boundary behaves coherently in the sense that—unlike generic material lines in a time-dependent flow—it does not stretch or form filaments over the time-period used in its identification. Hence, the coherent vortex boundary encloses fluid that stays inside the vortex, coherently separated from the ambient fluid. The vortex fluid region serves as a Lagrangian control volume that allows us to track vorticity and linear momentum and monitor the vortex formation process. We relate the vorticity and momentum history to the swimming dynamics and find that fish's momentum oscillations can be recovered from the momentum of coherent Lagrangian vortices for steady swimming.

The outline of the paper is a follows. In Sec. II, we describe the flow simulation and the detection method for coherent Lagrangian vortices. Section III comprises the results for the C-start and for steady swimming, and our conclusions are presented in Sec. IV.

II. METHODS

A. Flow simulation

In the fluid domain, we solve the incompressible 2D Navier–Stokes equations

$$\nabla \cdot \mathbf{u} = 0, \quad \frac{\partial \mathbf{u}}{\partial t} + (\mathbf{u} \cdot \nabla)\mathbf{u} = -\nabla p + \nu \nabla^2 \mathbf{u}, \quad (1)$$

where $\mathbf{u}$ and p are the fluid velocity and pressure, respectively, and ν is the kinematic viscosity. To account for the presence of the swimmer, we apply the no-slip boundary condition at the interface between the fluid and the body, to match the fluid velocity $\mathbf{u}$ to the local body velocity $\mathbf{u}_s$. The effect of the fluid onto the body is governed by Newton's equations of motion

$$m_s \ddot{\mathbf{x}}_s = \mathbf{F}^H, \quad d(I_s \theta_s)/dt = M^H, \quad (2)$$

where $\mathbf{F}^H$ and M^H are the hydrodynamic force and torque exerted by the fluid on the body, characterized by center of mass $\mathbf{x}_s$, angular velocity θ_s, mass m_s, and moment of inertia I_s. The body moving under (2) creates time-varying boundary conditions for (1).

The numerical method to discretize Eqs. (1) and (2) is a remeshed vortex method, with a penalization technique to account for the no-slip boundary condition and a projection method to incorporate the forces from the fluid onto the body.[4] The swimmer's geometry is represented with the characteristic function χ_s ($\chi_s = 1$ inside the body, $\chi_s = 0$ outside, and mollified at the interface), and its gait is imposed by a deformation velocity field $\mathbf{u}_{\text{def}}$. In this work, we employ the multiresolution implementation of this algorithm, which is open-source and has been discussed in Gazzola *et al.*[6] and Rossinelli *et al.*[18]

All simulations are performed in a unit square domain with effective resolution $16\,384 \times 16\,384$ and swimmer's length of $L = 0.05$. The refinement and compression tolerances are, respectively, 10^{-4} and 10^{-6}; the Lagrangian Courant-Friedrichs-Levy (CFL) condition for convergence is set to LCFL $= 0.01$; and the penalization constant is $\lambda = 10^4$. The simulations of the C-start are performed with swimmer's shape and midline kinematics as in Gazzola *et al.*,[5] with Reynolds number $Re = (L^2/T_{\text{prop}})/\nu = 550$, where T_{prop} is the period of the propulsive stroke. The steady-state simulations are performed with an anguilliform swimmer,[12] with Reynolds number $Re = (L^2/T_f)/\nu = 7143$, where T_f is the flapping period.

B. Coherent Lagrangian vortices

Coherent Lagrangian vortices are regions enclosed by outermost members of nested families of λ-lines.[11] λ-lines are curves that uniformly stretch or shrink by a small amount over a predefined finite time interval. Outermost closed λ-lines define the boundaries of coherent fluid patches and, in particular, the boundaries of coherent vortices. Since each segment of the coherent vortex boundary stretches by the same amount, filamentation and the break-away of material are prevented. Here, we review the necessary definitions and shortly describe the detection of λ-lines in a two-dimensional unsteady velocity field $v(x, t)$.

The evolution of a fluid trajectory is given by

$$\dot{x} = v(x, t).$$

A trajectory is denoted $x(t; x_0, t_0)$, with the initial position x_0 at time t_0. The flow map is

$$F_{t_0}^t(x_0) := x(t; t_0, x_0),$$

which maps initial positions to current positions at time t. The finite time $T = t - t_0$ is predefined and plays the role of the required coherence time for the coherent vortex boundary. The Cauchy–Green strain tensor

$$C_{t_0}^t(x_0) = [\nabla F_{t_0}^t(x_0)]^T \nabla F_{t_0}^t(x_0)$$

measures Lagrangian strain along trajectories and has eigenvalues and eigenvectors,

$$C_{t_0}^t \xi_i = \lambda_i \xi_i, \quad 0 < \lambda_1 \leq \lambda_2, \quad i = 1, 2.$$

As derived by Haller and Beron-Vera,[11] λ-lines are trajectories of one of the two vector fields

$$\eta_{\pm}^{\lambda} = \sqrt{\frac{\lambda_2 - \lambda^2}{\lambda_2 - \lambda_1}} \xi_1 \pm \sqrt{\frac{\lambda^2 - \lambda_1}{\lambda_2 - \lambda_1}} \xi_2.$$

Any trajectory segment of $\eta_{\pm}^{\lambda}$ stretches by a factor of λ under the flow map $F_{t_0}^t$. We obtain λ-lines by integrating

$$r'(s) = \eta_{\pm}^{\lambda},$$

where $r'(s)$ is a tangential vector to the λ-line which is parametrized by its arc length as $r(s)$. Closed λ-lines are the solutions to the variational principle of stationary averaged Lagrangian strain.[11]

λ is a parameter close to one, namely, the stretching factor for the coherent vortex boundaries. To detect coherent vortex boundaries, we vary λ in the range [0.95,1.05], i.e., we allow for maximally 5% stretching or shrinking of the curve. For each λ-value, we seek closed orbits in the vector fields $\eta_{\pm}^{\lambda}$, and define the outermost such closed orbit as the Lagrangian vortex boundary. A detailed description of the individual steps of the algorithm along with descriptive examples are given by Onu *et al.*[15] The associated MATLAB toolbox *LCS Tool* is available at https://github.com/jeixav/LCS-Tool.

The numerical advection of the detected vortex boundary lines in the simulated flow field has to be accurate. Therefore, the relative tolerance of the employed Matlab ode45 function has been set to 10^{-8} and additional points are added to the vortex polygons when the distance between neighbor points exceeds a threshold. Linear interpolation in time and space is sufficient, since the numerical data set has a high spatial and temporal resolution. The critical location for advection is the fish boundary: in case of insufficient accuracy, advected material lines may cross the fish boundary.

For the plots and diagrams, vorticity is computed from the velocity field with finite differences. The circulation Γ of the vortex fluid is obtained as $\Gamma = A \langle \omega \rangle_A$, where A is the area and $\langle \omega \rangle_A$ is the mean vorticity of the enclosed fluid region. Linear momentum is obtained as $\mathbf{p} = \rho A \langle \mathbf{u} \rangle_A$, where $\langle \mathbf{u} \rangle_A$ is the mean velocity, and density $\rho = 1$.

We consider a self-propelled body of constant area and unit density in an infinite 2D fluid, with no-slip boundary conditions on the body surface. In this case, the force of the fluid onto the body is given as

$$\mathbf{F}^H = m_s \ddot{\mathbf{x}}_s = -\frac{d}{dt} \int_{V_\infty(t)} \mathbf{u} \, dV - \oint_{S_\infty} p \hat{\mathbf{n}} \, dS,$$

where V_∞ is the region of the domain occupied by fluid, S_∞ is the bounding surface of the domain at infinity, and $\hat{\mathbf{n}}$ is the normal vector to that surface.[14,19] The left-hand side of the equation is obtained by differentiating the time history of the center-of-mass velocity of the swimmer. On the right hand side, the pressure integral cannot be calculated numerically with the current method. However, we found that neglecting the pressure term and restricting the volume integral to the computational domain only introduces a discrepancy in the momentum balance of $\sim$10% or smaller. This supports our approach of investigating to what extent the momentum change of the swimmer can be attributed to that of the coherent structures in the swimmer's wake.

III. RESULTS AND DISCUSSION

A. C-start

For the C-start maneuver, coherent vortices are detected at time $t_0 = 1.25$ with an integration time of $T = 0.5$. Figure 1 shows the detected vortex boundaries at the beginning and end of the coherent phase at times t_0 and $t_0 + T$. As guaranteed by the theory of coherent Lagrangian vortices, no filamentation or material break-away occurs along the advected curves over this period (inspect the dashed–dotted curves). The time t_0 corresponds to the time of the second tail stroke cycle when the second vortex pair (#4 and #5) is shed. The first vortex pair (#2 and #3), generated when the C-shape is straightened, is shed at $t \sim 0.65$. With this choice of t_0 and T, the first and the second vortex pairs are included in the analysis, but the major acceleration of the swimmer is due to the first vortex pair. Vortex #1 is generated during the preparatory stroke when the fish bends from a straight line to the C-shape. Its momentum contribution is small, rather opposing propulsion.

In order to obtain time series of vorticity and linear momentum of the vortex fluid, the vortex boundaries are advected with the flow over the whole time interval of the C-start maneuver, $t = [0.0, 1.77]$. Figure 2 gives an overview of the temporal evolution of the material fluid regions during vortex formation. The fluid, finally forming the vortices, is initially stretched out to an elongated shape. Interestingly, fluid from both sides of the fish constitutes the vortex fluid, while vorticity with the same sign as in each final vortex is located only on one side. In the presented sequence, this effect can be best observed for vortex #4.

In the first shown snapshot at $t = 0.3$, a pocket of fluid (black, #6) is enclosed by the deformed vortex boundaries of the first vortex pair (#2, #3), corresponding to the white enclosed fluid region in Fig. 6 in Gazzola *et al.*[5] This fluid region constitutes the jet fluid that is expelled backwards inside the first vortex pair. It corresponds to the propulsive
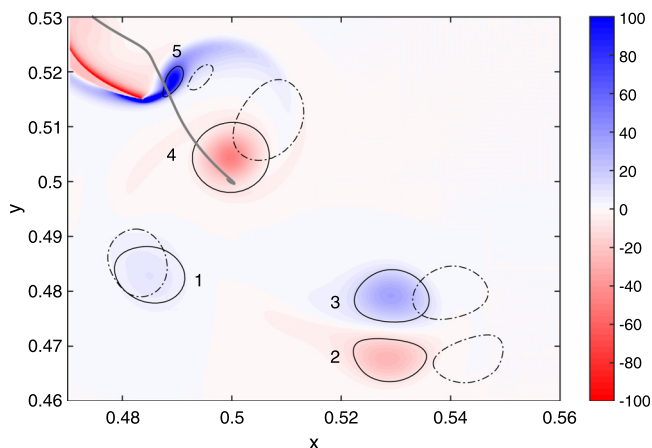

FIG. 1. Coherent vortex boundaries at $t_0 = 1.25$ (solid) with vorticity field and advected curves at $t_0 + T = 1.75$ (dashed–dotted). A short piece of the fish tail can be seen at the upper left corner. The trajectory of the fish's center of mass is drawn (solid, gray).
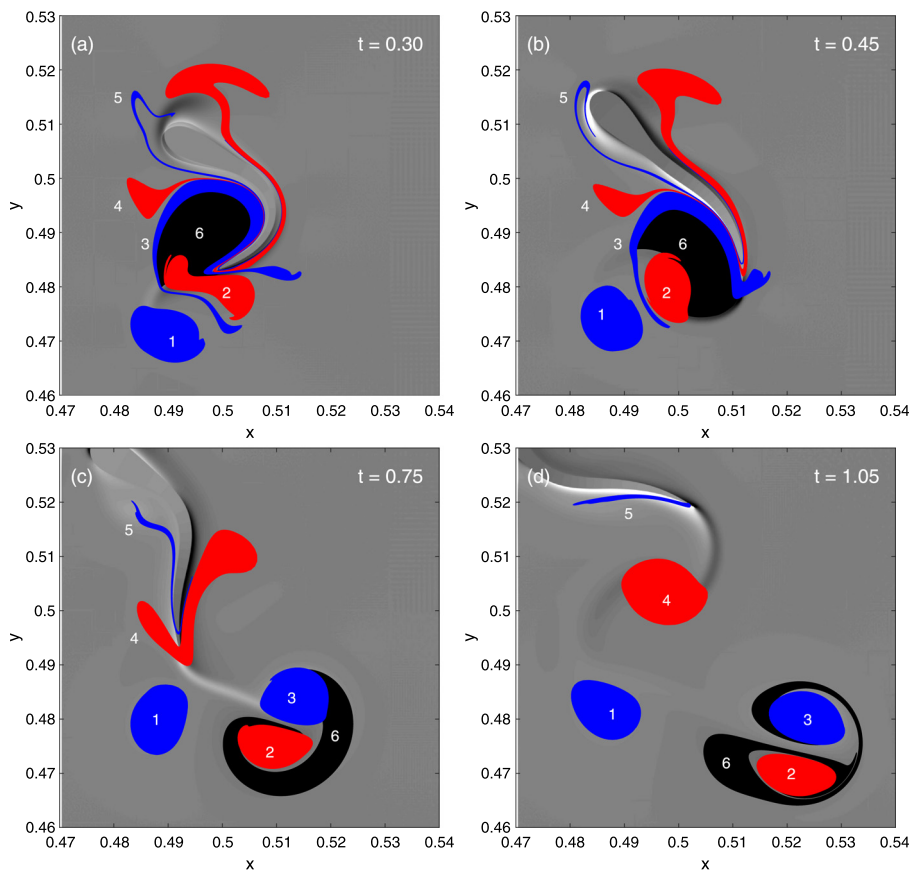
FIG. 2. Evolution of coherent vortex boundaries, clockwise rotation (red), anti-clockwise rotation (blue), and jet fluid (black). Vorticity is plotted in gray scales in the background to indicate the fish's position.

"Jet 2" in the experimental study with bluegill sunfish by Tytell and Lauder.[21] We define the boundary of the jet fluid at time $t = 0$ when the fluid is at rest. At this time, the bounding curves of vortex regions #2 and #3 are almost indistinguishably close, and the jet boundary is constructed by concatenating the corresponding segments of these two boundaries. The two segments are connected where they are closest. Although the jet fluid region does not transform into a coherent vortex, we add it to the five coherent vortex regions we consider, since it experiences a high acceleration during the start and is therefore a crucial part of the momentum balance.

The evolution of the vortex circulation $\Gamma(t)$ is shown in Fig. 3. Initially, the fluid is at rest and all vortices have zero circulation. The circulation increases slowly in the fish's boundary layer and rises abruptly right before the vortex is shed at the tail. This process is emphasized by Fig. 3(a), in which peak circulation corresponds to the shedding of the fluid region from the fish tail. The peak is followed by a slow decay in the wake due to viscosity. As an example, we show the decay of vortex region #2, and find that it fits well with the circulation decay of the viscous Lamb–Oseen vortex model[19] $\Gamma(t) = \Gamma_0[1 - e^{-\alpha(t-t_0)^{-1}}]$. Γ_0 is the peak circulation, t_0 is the time of vortex shedding, and $\alpha = r^2/(4\nu)$ is an inverse time constant, depending on the vortex radius r and the kinematic viscosity ν of the fluid. The Lamb–Oseen vortex is a circular two-dimensional vortex model with a Gaussian vorticity profile. The diffusive outflow of vorticity through a bounding material curve leads to the above decay of circulation with time. The peak circulation is similar for the coherent

vortices #2, #3, and #4, with values $\Gamma_0 \sim 3 \times 10^{-3}$. The circulation of vortex region #5 results smaller, since only a small core part of the vortex is detected as coherent in the prescribed time window, cf. Fig. 1. The preparatory vortex (#1) is also weaker with a peak circulation of $\Gamma_0 \sim 1 \times 10^{-3}$.

The gain of linear momentum of the fish in the accelerating phase of the C-start is closely linked to the generated coherent vortices. However, the primary contribution to the forward acceleration comes from the expelled jet of fluid. Figure 4 shows the temporal evolution of forward momentum for the six discrete fluid regions. The forward direction of the fish motion is defined by the trajectory of the center of mass of the fish over the interval [0, 0.47] (see trajectory in Fig. 1) and corresponds to an angle of $\sim45°$ to the vertical. Linear momentum of the fluid regions is projected onto the opposite direction to ease a direct comparison with the fish momentum.

The sum of forward linear momentum of all fluid regions (Fig. 4(a), black) is dominated by the momentum of the jet of fluid (magenta). Vortices #2 (cyan) and #3 (green) also contribute, but the forward linear momentum they carry is five times smaller. During the C-start, the fish gains its final momentum before $t = 0.5$, mainly during a steep rise of the momentum curve at $t = 0.3$, see Fig. 4(b) (red, solid). We note that both the fish's momentum and the (negative) momentum of the fluid regions (black) exhibit this steep rise approximately at $t = 0.3$. Consequently, the force impulse accelerating the fish is provided by the reaction force of the ejected fluid regions, in particular, by the jet fluid. The momentum of the fluid regions rises to values twice as high as
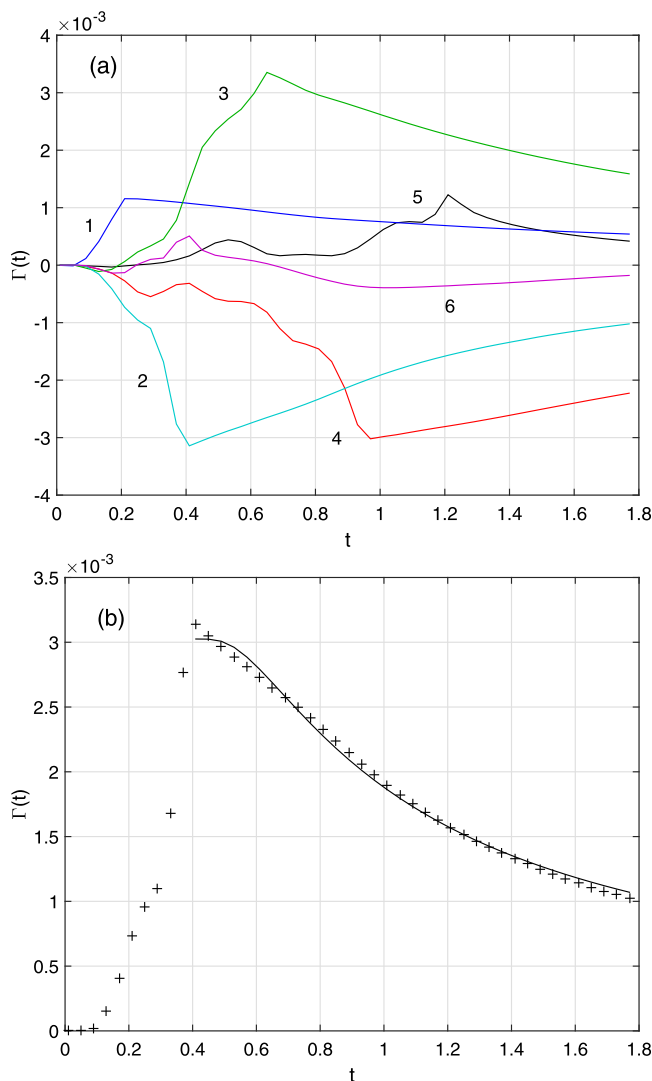
FIG. 3. (a) Circulation $\Gamma(t)$ of five C-start vortices (#1–5) and enclosed jet fluid (#6). (b) Viscous decay of circulation (absolute value) of vortex boundary #2 (black crosses), and curve fit with Lamb–Oseen vortex model [$\Gamma_0 = 3.0 \times 10^{-3}$, $t_0 = 0.37$] (solid line).
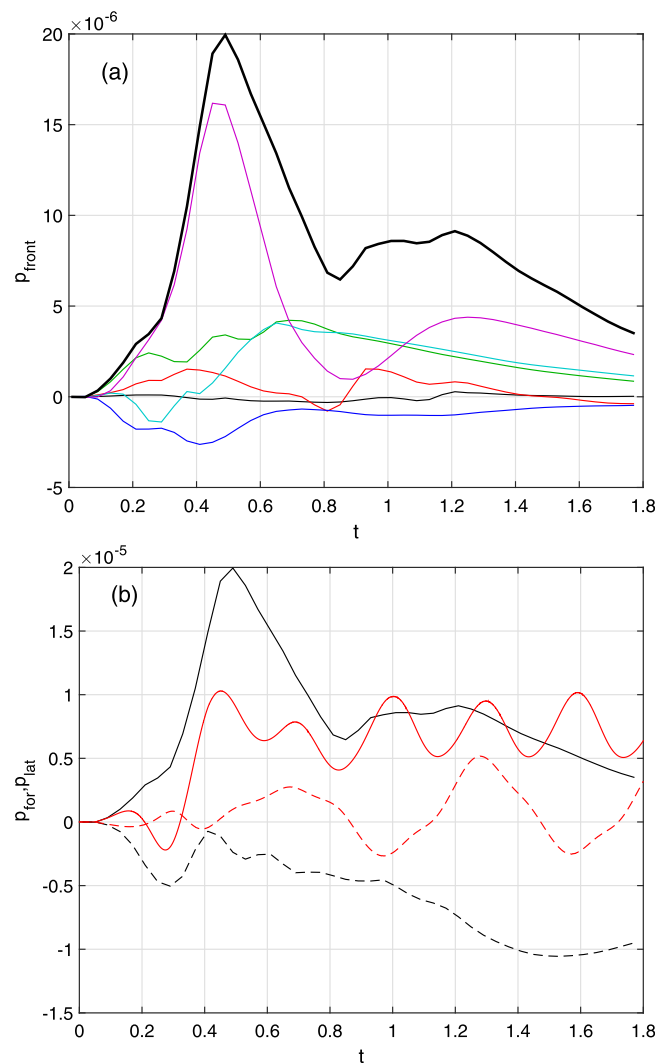

FIG. 4. Linear momentum of five vortices and jet region. (a) Linear momentum of fluid regions projected on negative swimming direction of fish. Same colors as in Fig. 3(a). First vortex pair (#2, cyan and #3, green) and jet fluid (#6, magenta). Sum of all fluid regions (black). (b) Linear momentum of fish (red) and total momentum of coherent fluid regions (black). Forward direction (solid) and lateral direction (dashed).

the fish's momentum. This imbalance could be explained by the added mass of the fish or the vortices[2] that we do not consider in the detected fluid regions. In the lateral direction, the momentum of the fish and the momentum of the fluid regions are not in balance, indicating that additional parts of the fluid have to be taken into account for a complete momentum balance of fluid and body.

In summary, the detection of coherent vortices in the C-start serves to define discrete Lagrangian fluid regions relevant for propulsion and to track their dynamics. Backward advection of these regions identifies a further jet region around which Lagrangian vortex boundaries accumulate beyond their coherence time.

B. Steady swimming

In the case of steady swimming, during the first cycle, a quarter-period sinusoidal ramp is employed, and for each swimming cycle afterwards, the swimmer's body deformation corresponds to anguilliform swimming.[12] We consider

the swimming mode of the fish as steady after an initial acceleration phase of eight cycles, corresponding to $t = 8.0$. After this period, the momentum of the center of mass of the fish is constant, apart from periodic body stroke-induced oscillations (cf. gray curve in Fig. 7(c)).

Coherent vortices are detected in the wake of the steady swimmer, one cycle after being shed from the tail, with an integration time also of one cycle, i.e., each coherent vortex has an individual initial time $t_0 = t_{shed} + 1.0$ and $T = T_c = 1.0$. The time t_{shed} is determined by visual inspection. We detect three consecutive vortices at $t_0 = [13.0, 13.5, 14.0]$ and advect the resulting boundary curves over the whole time interval of steady swimming [8.5 15.0].

The temporal evolution of the coherent vortex boundaries is shown in Fig. 5. Initially, the vortex fluid is stretched into an elongated shape with two larger patches on both sides of the swimmer. Similar lobes appear in Fig. 7 of Peng and Dabiri,[17] in FTLE-based hyperbolic LCS. This suggests that vortex fluid is embedded in the hyperbolic structures at
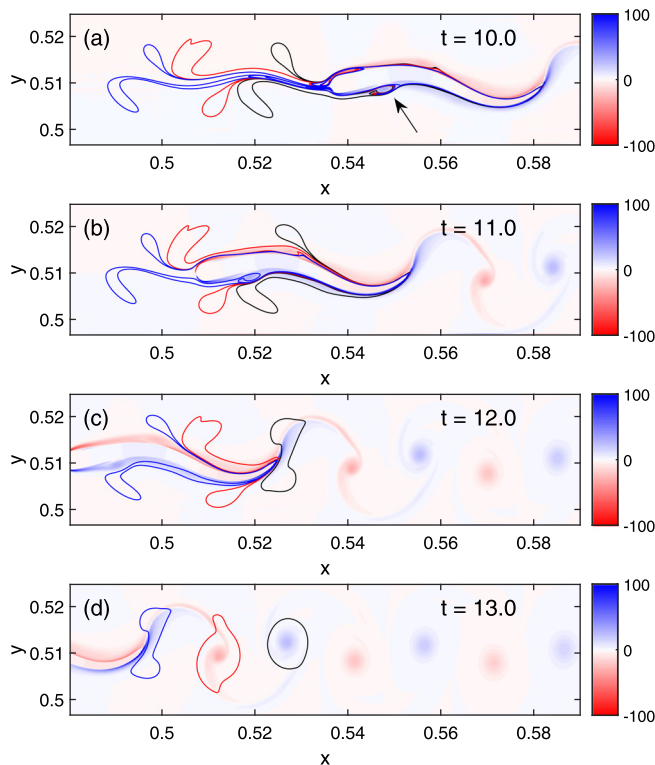
FIG. 5. Evolution of three coherent vortex boundaries during steady swimming. The arrow indicates a small vortex formed in the boundary layer behind the head.
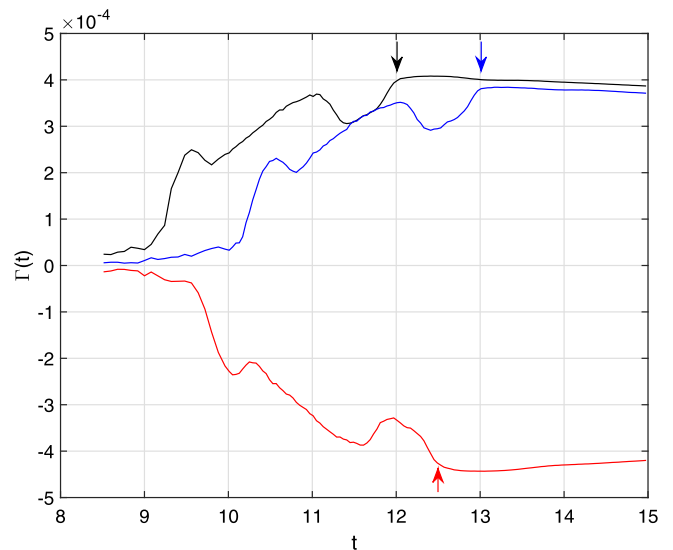

FIG. 6. Circulation $\Gamma(t)$ of three coherent vortices. Maximal circulation is attained when the vortex is shed from the tail at $t = [12.0, 12.5, 13.0]$ (arrows). Colors as in Fig. 5.

this location. It is surprising that the fluid patch on the side with opposite vorticity sign compared to the final vortex has a significant size, such that a large volume of fluid with opposite-sign vorticity is entrained into the final vortex during the shedding phase at the tail. The deformed fluid regions have qualitatively the same shape at $t = 0.3$, apart from translation and mirroring with respect to the horizontal axis, as expected for the periodic steady motion. Yet, a careful inspection reveals different details. This is because the detected circular vortex regions, at their individual t_0, have slightly different sizes, which may be related to an imperfect periodic flow. These small differences are propagated through the non-linear advection to earlier times.

Both fluid patches on either side of the fish are connected with a thin filament of negligible area. The filaments of the three vortices are arranged side by side, overlap with the boundary layer of the swimmer's skin, and exhibit a broader band of fluid in front of the swimmer. When the fish passes through the vortex regions, the contained fluid gains vorticity, and finally rolls up to a coherent vortex when shed at the tail. Figure 6 shows the circulation $\Gamma(t)$ of the three detected vortices. The circulation is practically zero when the fluid regions are initially at rest far upstream of the fish. Then, the circulation rises as the fish proceeds, until the vortex is shed, and viscous decay starts. Due to the periodic motion, the curves show the same behavior, as expected. Since they are associated with three consecutive vortices, all three curves are shifted in time by $\Delta t = 0.5$. The second vortex region (red) has a negative circulation, indicating the opposite sense of rotation compared to the first and third vortex region. The first

local maximum of circulation, for example, for the red curve at $t = 10.0$, corresponds to the vorticity generated in a small vortex behind the head (see arrow in Fig. 5).

Concerning the linear momentum balance, the steady swimming case differs from the accelerating C-start case. During steady swimming, the momentum of the fish, averaged over a flapping period, is constant, and therefore, the net momentum exchange with the fluid is null. However, oscillations in the forward momentum of the fish (in x-direction) exist due to the intermittent propulsion by tail strokes. These sinusoidal oscillations can be seen in Fig. 7(a) represented by the gray curve, the linear momentum of the fish. The curve is shifted by an arbitrary p_x-offset to ease visual comparison with the momentum of the vortex fluid.

The constant component of the linear momentum of the fish during steady swimming was gained during the initial acceleration phase prior to our analysis period. Therefore, we focus on the oscillations in the fish's forward momentum and relate them to the momentum of the coherent vortices. Fig. 7(a) shows the momentum time series of the fluid regions associated with the detected coherent vortices (thin black, red, and blue). Color-coded bars indicate the time when the vortex region goes past the head and when the vortex is shed at the tail. The momentum history of an individual fluid patch can be divided into three phases depending on the location of the fluid: upstream, alongside, or downstream of the fish.

In the first phase, starting from zero, the individual fluid region gains momentum in the swimming direction of the fish. This corresponds to the fluid being pushed forward due to the approaching swimmer, a part of the added mass of the body, which can be associated with a drag acting on the swimmer. In the second phase, after contact with the body, the fluid is accelerated backwards until it reaches zero momentum again, right before being shed by the tail. This phase is associated to thrust production. Note that the shedding times of the three vortices, $t_{shed} = [12.0, 12.5, 13.0]$, agree
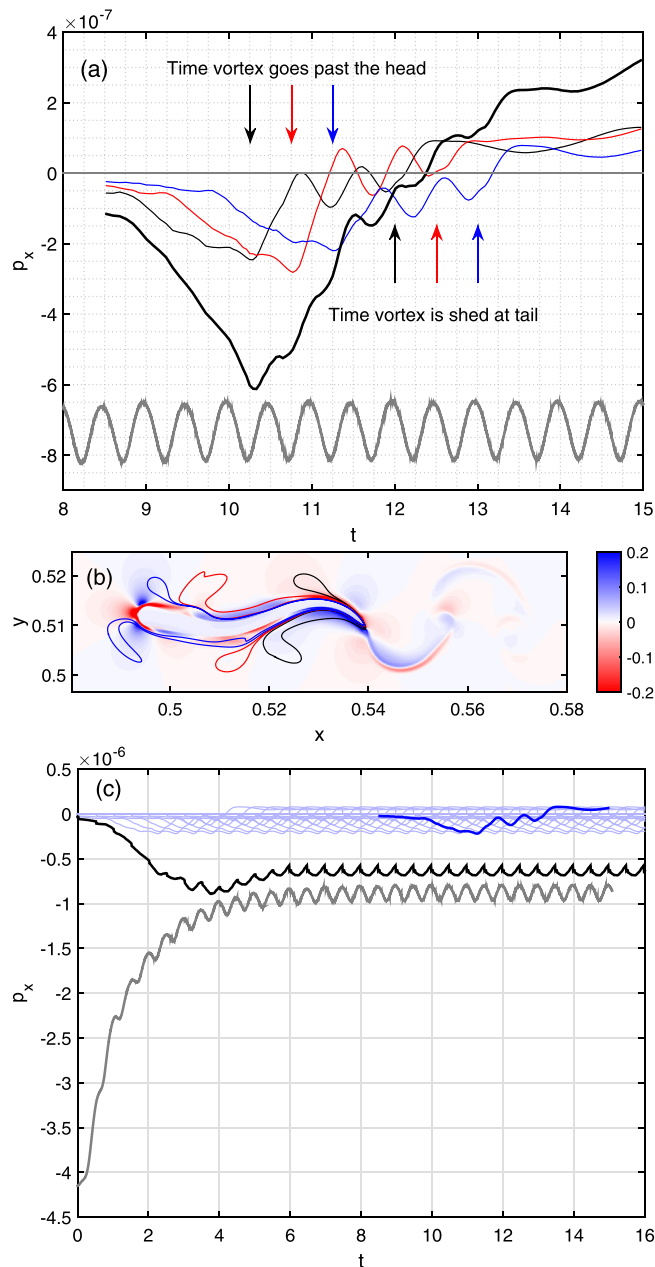
FIG. 7. (a) Linear momentum in x-direction p_x of the three consecutive coherent vortices (black, red, blue, thin line), sum of vortex momentum (bold, black), negative fish momentum p_x (bold, grey, with arbitrary offset added to ease visual comparison). The times when the vortex region goes past the head of the fish and when the vortex is shed at the tail are indicated by color-coded bars. Colors as in Fig. 5. (b) Instantaneous acceleration of fluid $a_x = dv_x/dt$ at $t = 11.5$. Blue (red) fluid is accelerated in positive (negative) x-direction and induces a thrust (drag) reaction force on the fish (or on the rest of the fluid). Accelerated and decelerated fluid regions alternate along the fish body. Thrust (drag) regions are found where the fish boundary is concave (convex). (c) Momentum evolution (black), obtained as the sum of periodically shifted momentum curves of a single vortex (blue). Shifting period $\tau = 0.5$. Linear momentum of fish (grey).

with the times when the momentum of the individual fluid regions attain zero momentum again. In the third phase, vortices in the wake possess small backward momentum, which slowly decays as the swimmer has passed.

The oscillations in the fish momentum have twice the frequency of the tail beat, i.e., $f_p = 2$, one acceleration-deceleration cycle per generated vortex. However, this frequency is not present in the momentum history of an individual vortex fluid region. The individual momentum curves have lower frequencies of typically $f_p \sim 4/3$. The oscillations occur when alternating drag and thrust regions along the fish propagate with the fish through the vortex material patches (Fig. 7(b)). Only if the momentum time series of several vortices is superposed (Fig. 7(a), bold black curve), the dominant frequency in the total momentum matches the frequency of the fish momentum. The dominant frequency of $f_p = 2$ can be seen in the bold black total momentum curve approximately over the range [10.25, 12.50].

To strengthen this observation, we construct a total momentum time series of the vortex fluid, by summing up a periodically shifted individual momentum curve. Figure 7(c) shows the individual momentum curve (blue), the copies shifted by 0.5 in time (faint blue), and the summed up total momentum (black). While it is not surprising that the resulting total momentum has a dominant period of 0.5 (by construction), it is noteworthy that the amplitude of the constructed total momentum is very similar to the amplitude of the oscillations of the fish momentum. Consequently, it seems that the oscillations in the fish momentum are balanced by the superimposed momentum time series of individual vortex regions.

Our results show that, by following the momentum history of a coherent vortex fluid region as a material entity, drag and thrust can be spatially and temporally separated to some extent. According to the momentum history, depicted in Fig. 7(a), an individual vortex fluid region is first accelerated in swimming direction upstream of the fish, acting as drag, and later accelerated in backward direction aside the fish, acting as thrust. Yet, the backward acceleration aside the fish is not monotonic. Regions of thrust and drag alternate along the undulating body (Fig. 7(b)). Thrust (drag) regions are located close to concave (convex) regions of the fish boundary. This is consistent with the C-start, where the thrust-generating accelerated fluid is located within the concave C-shaped body during the preparatory stroke. Since the vortex fluid is distributed along both sides of the fish body, it both covers drag and thrust regions when the fish passes. However, the net thrust effect can then be predominantly attributed to the fluid located in the concave sections of the fish's flexing body.

We wish to stress that in our analysis, we only considered a discrete set of coherent vortices, while non-negligible contributions of other parts of the fluid may have been overlooked. In particular, the jet fluid in close contact with the fish in-between the lobes of the vortex fluid in Fig. 5(a) could be relevant. Yet, the fact that the momentum of the vortex fluid alone can largely explain the momentum fluctuations of the fish suggests that complementary jet fluid regions predominantly carry lateral momentum that is of minor importance for propulsion.

IV. CONCLUSION

In this study, we quantify the contribution of discrete coherent Lagrangian vortices to the momentum balance of two different modes of swimming propulsion, impulsive C-start escape, and steady anguilliform swimming. For the

C-start, Gazzola *et al.*[5] report that the fluid region trapped inside the C-shape consists of a vortex pair and a low vorticity jet region. They find that bending the body into a C-shape is an optimal strategy for fast escapes, as it allows the fish to trap and accelerate the largest amount of fluid. We quantify the momentum transfer to the trapped fluid and show that the main contribution comes from the jet fluid region, initially enclosed by vortex fluid and finally expelled as a jet. For steady swimming, the amplitude and frequency of momentum oscillations of the fish are matched when the momentum records of individual vortex regions are periodically superposed. For an individual vortex region, a phase of drag production upstream of the fish can be separated from a phase of thrust production along the fish. Consistent with the C-start, thrust regions aside the fish are located where the body is concave suggesting a similar propulsion mechanism. The geometry of the deformed vortex fluid upstream of the swimmer, revealed by our method, can be of further interest when the swimmer interacts with vorticity from upstream obstacles, like a stationary bluff body[13] or other fish in fish schools.[4]

ACKNOWLEDGMENTS

[1] R. Bale, M. Hao, A. P. S. Bhalla, N. Patel, and N. A. Patankar, "Gray's paradox: A fluid mechanical perspective," Sci. Rep. **4**, 5904 (2014).

[2] J. O. Dabiri, "On the estimation of swimming and flying forces from wake measurements," J. Exp. Biol. **208**, 3519–3532 (2005).

[3] B. P. Epps and A. H. Techet, "Impulse generated during unsteady maneuvering of swimming fish," Exp. Fluids **43**, 691–700 (2007).

[4] M. Gazzola, P. Chatelain, W. M. van Rees, and P. Koumoutsakos, "Simulations of single and multiple swimmers with non-divergence free deforming geometries," J. Comput. Phys. **230**, 7093–7114 (2011).

[5] M. Gazzola, W. M. van Rees, and P. Koumoutsakos, "C-start: Optimal start of larval fish," J. Fluid Mech. **698**, 5–18 (2012).

[6] M. Gazzola, B. Hejazialhosseini, and P. Koumoutsakos, "Reinforcement learning and wavelet adapted vortex methods for simulations of self-propelled swimmers," SIAM J. Sci. Comput. **36**(3), B622–B639 (2014).

[7] M. A. Green, C. W. Rowley, and A. J. Smits, "The unsteady three-dimensional wake produced by a trapezoidal pitching panel," J. Fluid Mech. **685**, 117–145 (2011).

[8] G. Haller, "A variational theory of hyperbolic Lagrangian coherent structures," Physica D **240**, 574–598 (2011).

[9] G. Haller, "Lagrangian coherent structures," Annu. Rev. Fluid Mech. **47**, 137–162 (2015).

[10] G. Haller and G. Yuan, "Lagrangian coherent structures and mixing in two-dimensional turbulence," Physica D **147**, 352–370 (2000).

[11] G. Haller and F. J. Beron-Vera, "Coherent Lagrangian vortices: The black holes of turbulence," J. Fluid Mech. **731**, R4 (2013).

[12] S. Kern and P. Koumoutsakos, "Simulations of optimized anguilliform swimming," J. Exp. Biol. **209**, 4841–4857 (2006).

[13] J. C. Liao, D. N. Beal, G. V. Lauder, and M. S. Triantafyllou, "Fish exploiting vortices decrease muscle activity," Science **302**, 1566–1569 (2003).

[14] F. Noca, D. Shiels, and D. Jeon, "Measuring instantaneous fluid dynamic forces on bodies, using only velocity fields and their derivatives," J. Fluid Struct. **11**, 345–350 (1997).

[15] K. Onu, F. Huhn, and G. Haller, "LCS Tool: A computational platform for Lagrangian coherent structures," J. Comput. Sci. **7**, 26–36 (2015).

[16] J. Peng, J. O. Dabiri, P. G. Madden, and G. V. Lauder, "Non-invasive measurement of instantaneous forces during aquatic locomotion: A case study of the bluegill sunfish pectoral fin," J. Exp. Biol. **210**, 685–698 (2007).

[17] J. Peng and J. O. Dabiri, "The 'upstream wake' of swimming and flying animals and its correlation with propulsive efficiency," J. Exp. Biol. **211**, 2669–2677 (2008).

[18] D. Rossinelli, B. Hejazialhosseini, W. M. van Rees, M. Gazzola, M. Bergdorf, and P. Koumoutsakos, "MRAG-I2D: Multi-resolution adapted grids for vortex methods on multicore architectures," J. Comput. Phys. **288**, 1–18 (2015).

[19] P. G. Saffman, *Vortex Dynamics* (Cambridge University Press, New York, 1992).

[20] W. W. Schultz and P. W. Webb, "Power requirements of swimming: Do new methods resolve old questions?," Integr. Comp. Biol. **42**, 1018–1025 (2002).

[21] E. D. Tytell and G. V. Lauder, "Hydrodynamics of the escape response in bluegill sunfish, *Lepomis macrochirus*," J. Exp. Biol. **211**, 3359–3369 (2008).